RSC Advances



PAPER

View Article Online
View Journal | View Issue



Cite this: RSC Adv., 2025, 15, 24851

One-step co-precipitation synthesis, characterization, and enhanced photocatalytic performance of CaO/TiO₂-supported γ -Al₂O₃ nanocomposites (NCs) in wastewater treatment

Emaan Alsubhe *

Hybrid nanocomposites (NCs) have garnered significant attention for their potential applications, including photocatalysis, energy storage, and gas-sensing. This study reports the preparation, characterization, and photocatalytic activity of calcium oxide/titanium dioxide/gamma alumina (CaO/ TiO_2/γ - Al_2O_3) NCs fabricated through a one-step co-precipitation processes. Different analytical tools, including X-ray diffraction (XRD), transmission electron microscopy (TEM), scanning electron microscopy (SEM) with energy dispersive X-ray spectroscopy (EDX), Raman spectroscopy, Fourier transform infrared spectroscopy (FTIR), photoluminescence spectroscopy (PL), ultraviolet-visible spectroscopy (UV-Vis), and dynamic light scattering (DLS), were carefully applied to examine the structural, morphological, and optical properties of the obtained NPs and NCs. The XRD results exhibited an important improvement in the crystallinity and phase purity of γ-Al₂O₃ NPs with supporting CaO NPs and TiO₂ NPs. TEM and SEM analyses verified that the synthesized NPs and NCs have a spherical morphology with a decrease in particle size from 9.50 \pm 1.2 nm to 8.21 \pm 2.1 nm after the addition of CaO NPs. EDX analysis revealed the presence of the elements calcium, titanium, aluminum and oxygen (Ca, Ti, Al, and O) within the CaO/TiO $_2$ / $_7$ -Al $_2$ O $_3$ NCs. Raman and FTIR spectra determined the functional groups of the prepared samples. The reduction of the PL intensity indicates that the recombination of the electron-hole pairs is decreased upon adding CaO NPs and TiO₂ NPs. DLS results showed the surface charge and particle distribution of the synthesized NPs and NCs. The degradation of methylene blue (MB) dye under ultraviolet UV irradiation for 200 min was employed to examine the photocatalytic activity of these samples. As shown in the results, the photocatalytic activity of γ -Al₂O₃ NPs, TiO₂/ γ -Al₂O₃ NCs, and CaO/TiO₂/ γ -Al₂O₃ NCs reached up to 45%, 79%, and 98%, respectively. It can be observed that the $CaO/TiO_2/\gamma$ - Al_2O_3 NCs achieved higher degradation than the individual samples. These improvements in the observed photocatalytic performance can be linked to various parameters, including the charge separation and increased surface area. The incorporation of CaO and TiO2 into γ-Al2O3 enhances its photocatalytic efficiency by improving charge separation and expanding the surface area. They also promote light absorption and surface reactivity, which help suppress and increase the number of available active sites. These results highlight that the $CaO/TiO_2/\gamma - Al_2O_3$ NCs can enhance photocatalytic performance, especially the degradation of organic pollutants in wastewater. This study is an important step toward further research to apply these NCs in medical therapy.

Received 18th May 2025 Accepted 27th June 2025

DOI: 10.1039/d5ra03493k

rsc.li/rsc-advances

1. Introduction

Environmental technologies have drawn much attention to photocatalysis, which is a promising approach for degrading organic pollutants.^{1,2} The current elimination of emerging contaminants, such as pollutant dyes, and antibiotics, in rivers, lakes, and seas remains a challenge for wastewater treatment

Department of Physics, College of Science, Taibah University, Yanbu 46423, Saudi Arabia. E-mail: esobhe@taibahu.edu.sa

processes.³⁻⁵ However, the serious environmental problem of organic pollutants in water bodies has attracted and driven significant research studies toward finding efficient and sustainable methods to eliminate these pollutants using nanomaterials in different forms.^{6,7} Among these nanomaterials, γ -Al₂O₃ nanoparticles (NPs) have been widely studied as one approach in wastewater treatment processes owing to their superior physicochemical properties, such as good stability and excellent photocatalysis efficiency under UV and visible irradiation.^{8,9} Nevertheless, it has many limitations, such

as a wide band gap (\sim 3.6 eV), which plays a role in decreasing its photocatalytic activity due to a high rate of recombination of pairs (electrons (e⁻) and holes (h⁺)).¹⁰ To address these limitations, different approaches have been applied to improve its photocatalytic activity, including coupling with other metal oxide nanoparticles (NPs) or doping with metal ions to create a new nanocomposite.^{11,12} Moreover, the γ -Al $_2$ O $_3$ NP mixtures support different metal oxide NPs, such as ZnO,¹³ ZrO $_2$,¹⁴ TiO $_2$,¹⁵ CaO,¹⁶ CuO,¹⁷ and SnO $_2$ NPs,¹⁸ which have attracted increasing interest because of their exceptional properties, including high surface area and strong stability.

To optimize the photocatalytic properties of the hybrid metal oxide NCs, synthesis plays a crucial role. Likewise, chemical, physical, and biological techniques have been widely developed to prepare hybrid metal oxide NPs like γ-Al₂O₃ NPs to enhance their potential applications. For example, Huang et al.19 used the co-precipitation route to synthesize N-TiO₂/ γ -Al₂O₃ nanostructures for improved photodegradation (92.5%) of 2,4dichlorophenol dye under fluorescence irradiation (60 W). In another instance, the sol-gel process was applied to prepare Fedoped TiO₂/γ-Al₂O₃ NCs with high photocatalytic activity compared with pure γ-Al₂O₃. Mahdi et al.²⁰ investigated the use of clove extract to prepare γ-Al₂O₃ NPs, revealing that they exhibited high antimicrobial activity and effective removal of metal ions from water. Dubadi et al.21 reported that various metal oxide NPs, such as Fe₂O₃, CuO, ZnO, Bi₂O₃, and Ga₂O₃, have been combined with γ-Al₂O₃ using liquid-assisted grinding to synthesize nanocomposites (NCs) with high aromatic pollutant degradation. Moreover, Kudla et al.22 prepared Zr and Mg-doped γ-Al₂O₃ NCs using hydrothermal treatment to enhance the thermal stability. The Cu, Pd, Ni, Co/ γ-Al₂O₃ demonstrated high photodegradation of the methylene blue, 4-nitrophenol, nitrite, and nitrate dyes compared to pure γ-Al₂O₃.23 In the past few years, as a result of their physicochemical characteristics, the enhancement of photocatalyst materials has attracted significant attention in potential applications. Furthermore, several studies reported that different oxide compounds of metal (e.g., TiO₂, CuO, SnO₂, ZnO and NiO) have been combined with other metal oxide NPs to improve their photocatalytic performance in environmental remediation and wastewater treatment.24,25 Kanwal et al.26 have discovered that Mn₂O₃/γ-Al₂O₃ NCs exhibit better-quality photocatalytic activity compared with the pure components. As a result, the coprecipitation method provides a simple, cost-effective and scalable route to synthesize nanocomposites with controlled particle size, uniform composition and high purity, making it superior to other methods such as hydrothermal treatment and sol-gel synthesis for practical uses. 19,27

The present work focuses on fabricating CaO/TiO $_2/\gamma$ -Al $_2$ O $_3$ as a catalyst for enhancing photocatalytic performances, particularly the degradation of organic contaminants. The chemical coperception process was successfully applied to synthesize samples. The physicochemical properties of the prepared samples were investigated through analytical methods, including XRD, Raman, SEM with EDX, FTIR, PL, and DLS. The degradation of the methylene blue (MB) dye under UV light was used to investigate the photocatalytic efficiency of the catalysts.

2. Experimental part

2.1 Chemicals and methods

In these experiments, all chemical materials were utilized without further purification. Gamma-alumina $(\gamma\text{-Al}_2O_3)$ (99.95% trace metals), titanium(IV) butoxide (Ti(O-But)_4), calcium nitrate (Ca(NO_3)·4H_2O), sodium hydroxide (NaOH), and methylene blue (MB) dye were supplied from Sigma-Aldrich Company (St. Louis, MO, USA). In all experiments, distilled water and ethanol were employed as solvents.

2.2 Preparation of CaO/TiO₂/γ-Al₂O₃ NCs

The chemical co-precipitation process was successfully applied to prepare $CaO/TiO_2/\gamma-Al_2O_3$ (15:15:70) nanocomposites (NCs) using the following procedures as a one-step method. Firstly, 0.07 mol of γ-Al₂O₃ NPs was added to 30 mL of water and a magnetic stirrer in a 250 mL round-bottomed flask. Next, 0.015 mol of Ti(O-But)4 was mixed with 10 mL of ethanol and added to the above solution under stirring. After that, 0.015 mol of Ca(NO₃)·4H₂O was mixed with the prior solution, followed by stirring for 1 h. Then, 0.031 mol of NaOH in 15 ml water was slowly added to the mixture solution with stirring at 65 °C for 5 h. Following filtration, the sample was repeatedly washed with ethanol and water, then dried in the oven at 60 °C for 24 h. The dried powder was calcined at 500 °C under air for 4 h to produce CaO/TiO₂/γ-Al₂O₃ NCs. By applying the same procedures, TiO₂/ γ -Al₂O₃ NCs (30:70) were further produced with amount of γ -Al₂O₃ (0.1 mol) and Ti(O-But)₄ (0.03 mol), and without Ca(NO₃) $4H_2O$.

2.3 Characterization tools

Several analytical techniques were used to investigate the enhanced physicochemical properties. X-ray diffraction (XRD) analysis (AXRD Benchtop, Proto Manufacturing, Inc., USA) was used to examine the crystalline and phase purity properties. The surface morphology, structure, particle size, and elemental compositions of the synthesized samples were further examined via transmission electron microscopy (TEM) (JEM-2100F, JEOL, Inc., Tokyo, Japan) and scanning electron microscopy (SEM) (JSM-7600F, JEOL, Inc., Tokyo, Japan) with energydispersive X-ray spectroscopy (EDX) techniques. Raman spectroscopy (STR 500 Confocal Micro Raman spectrometer) was used to assess the crystal structure of the prepared samples. Likewise, FTIR spectroscopy (PerkinElmer Paragon 500, USA) was used to determine the functional groups of the synthesized samples. PL spectroscopy (Hitachi F-4600) was applied to study the optical properties. The surface charges and particle distribution of the samples were evaluated through dynamic light scattering (DLS) (Malvern, Worcestershire, UK).

2.4 Photocatalytic experiments

We used methyl blue (MB) dye to evaluate the γ -Al₂O₃ NPs, TiO₂/ γ -Al₂O₃ NCs, and CaO/TiO₂/ γ -Al₂O₃ NCs as catalysts. Initially, 10 ppm of the MB solution was mixed with 40 mg of each catalyst. Then, the mixed solution was placed under dark

Paper

conditions with magnetic stirring for 30 minutes to test the absorption–adsorption equilibrium. After that, it was irradiated with a UV light source for 200 minutes. After being exposed for 20 minutes, a micropipette was used to take 3.0 mL of the mixture solution. The sample was centrifuged at 4000 rpm for 10 minutes to remove it from the dye solution. Subsequently, the absorbance of the MB solution was measured using UV-Vis spectroscopy. The dye degradation efficiency was measured using the following eqn (1):

Degradation efficiency (%) =
$$[(C_0 - C_t)/C_0] \times 100$$
 (1)

where C_0 is the first absorbance of the MB dye without samples, and C_t is the absorbance at a specific exposure time (t). The constant rate (K) of the MB degradation was calculated using eqn (2) as follows:

$$K_{t} = \ln\left[C_{0}/C_{t}\right] \tag{2}$$

where K is the constant rate of degradation, C_0 is the first absorbance of the MB dye without samples, and C_t is the absorbance at exposure time (t). Under the same experimental conditions, cyclic photocatalysis tests were performed using CaO/TiO₂/ γ -Al₂O₃ NCs. After dark adsorption, a 200 min photocatalytic decomposition of MB was applied, and the process was repeated four times. After each cycle, the photocatalyst was separated from the MB solution by centrifugation and washed three times with ethanol. The powder was then dried at 60 °C for 24 h before being reused.

3. Results and discussions

3.1 XRD study

XRD analysis was performed to investigate the crystallinity and phase composition of the prepared samples. Fig. 1 depicts the XRD pattern of the produced γ-Al₂O₃ NPs, TiO₂/γ-Al₂O₃ NPs, and $CaO/TiO_2/\gamma$ -Al₂O₃ NPs. In Fig. 1a, the observed peaks of the γ -Al₂O₃ NPs were at $2\theta = 32^{\circ}$ (220), 37° (311), 39° (222), 46° (400), 61° (511), and 67° (440). These peaks confirm the structure of γ -Al₂O₃, as demonstrated in previous studies.^{28,29} In the analysis of the TiO₂/γ-Al₂O NCs (Fig. 1b), several new peaks were detected at $2\theta = 25^{\circ}$ (101), 47° (200), 55° (105), 63° (204) and assigned to TiO2, similar to earlier studies.30-32 Additionally, peaks corresponding to the presence of γ -Al₂O₃ were observed. These findings confirm the successful combination of TiO₂-Al₂O₃ NCs. In contrast, the XRD spectra of CaO/TiO₂/γ-Al₂O₃ NCs (Fig. 1c) exhibited sharp peaks compared to those of both γ-Al₂O₃ NPs and TiO₂/γ-Al₂O₃ NCs, indicating a higher degree of crystallinity in the CaO/TiO₂/γ-Al₂O₃ NCs. Significantly, new peaks appeared at 31° (111), 44° (200), 44° (220) and 50° (220), which agrees with previous studies of CaO. 33-35 Additionally, the peaks at 25°, 37°, 45° and 67° confirm the synthesis of CaO/ TiO_2/γ -Al₂O₃ NCs. The average crystalline size at 67° (440) for all synthesized samples were calculated by Scherrer's eqn (3), which is given as follows:28

Crystallite size
$$(D) = \frac{K\lambda}{\beta \cos \theta}$$
 (3)

where D is the crystallite size (in nanometers), and K is the shape factor (0.9). λ is the X-ray wavelength (Cu-K α radiation, $\lambda=1.5406$ Å), β is the full width at half maximum (FWHM) of the diffraction peak in radians, and θ is the diffraction angle (in radians). It can be observed that the average crystallinity size of the prepared γ -Al $_2$ O $_3$ NPs, TiO $_2$ / γ -Al $_2$ O $_3$ NCs, and CaO/TiO $_2$ / γ -Al $_2$ O $_3$ NCs were 3.2 \pm 1.4 nm, 2.4 \pm 0.8 nm, and 2.7 \pm 0.5 nm, respectively, as illustrated in Table 1. These values indicate that the addition of TiO $_2$ and CaO played a role in enhancing the crystal structure. The XRD spectra confirmed that CaO/TiO $_2$ / γ -Al $_2$ O $_3$ NCs could be applied in potential applications, such as photocatalysis, gas-sensing, and energy storage. The obtained XRD results were in good agreement with earlier investigations. 29,31,33

3.2 TEM analysis

Fig. 2a-i displays the TEM images, HRTEM images, and the particle size for Al₂O₃ NPs, TiO₂/ γ -Al₂O₃ NCs, and CaO/TiO₂/ γ -Al₂O₃ NCs. As illustrated in Fig. 2a and c, the TEM image of the pure γ-Al₂O₃ NPs was found to be spherical in shape with an average particle size of 9.55 \pm 1.2 nm, similar to previous studies. Fig. 2b shows that the d-spacing of γ -Al₂O₃ NPs was 0.238 nm, which matched with the XRD data (Fig. 1a). For TiO₂/ γ -Al₂O₃ NCs (Fig. 2d-f), the particle size of NCs has a spherical shape with a decreased size (7.60 \pm 0.9 nm) compared with pure γ -Al₂O₃ NPs. The decrease in particle size is likely due to the interaction of TiO₂ with the surface of γ-Al₂O₃, stabilizing smaller particles and preventing their agglomeration. 38,39 It was observed that the d-spacing values for TiO₂/γ-Al₂O₃ were 0.193 nm and 0.321 nm for γ-Al₂O₃ NPs and TiO₂, respectively.40,41 These values indicate that TiO₂/γ-Al₂O₃ NCs were successfully prepared. Additionally, Fig. 2g shows the TEM image of the prepared CaO/TiO₂/γ-Al₂O₃ NCs. As a result, the particles of γ-Al₂O₃ NPs exhibited more agglomeration with increased size (8.21 \pm 2.1 nm) after the addition of the CaO compared to an individual sample, as shown in Table 1. Recent studies have reported that the crystallinity refers to the degree of order or regularity in the arrangement of atoms within a material, while the particle size (or crystallite size) refers to the physical size of the individual crystalline domains. 42,43 As observed in the XRD data, the crystallites of the CaO/TiO₂/γ- Al_2O_3 NCs are smaller (2.7 nm) compared to the γ - Al_2O_3 NPs and TiO₂/γ-Al₂O₃ NCs. This indicates that the CaO addition leads to smaller, yet well-ordered crystalline domains. Fig. 2i demonstrates the d-spacing of the structure, which was 0.235 nm, 0.312 nm, and 0.241 nm for γ -Al₂O₃ NPs TiO₂ NPs and CaO NPs, respectively. The TEM results were in good agreement with earlier studies, 9,39,44 and matched well with the XRD data (Fig. 1a-c).

3.3 SEM with EDX analysis

The SEM and EDX analyses was performed on the fabricated samples to study their surface morphology properties, as illustrated (Fig. 3a–d). It can be observed in Fig. 3a that the pure γ -Al₂O₃ NPs have a spherical shape with less agglomerations. As illustrated in Fig. 3a–c, the structural morphologies of the

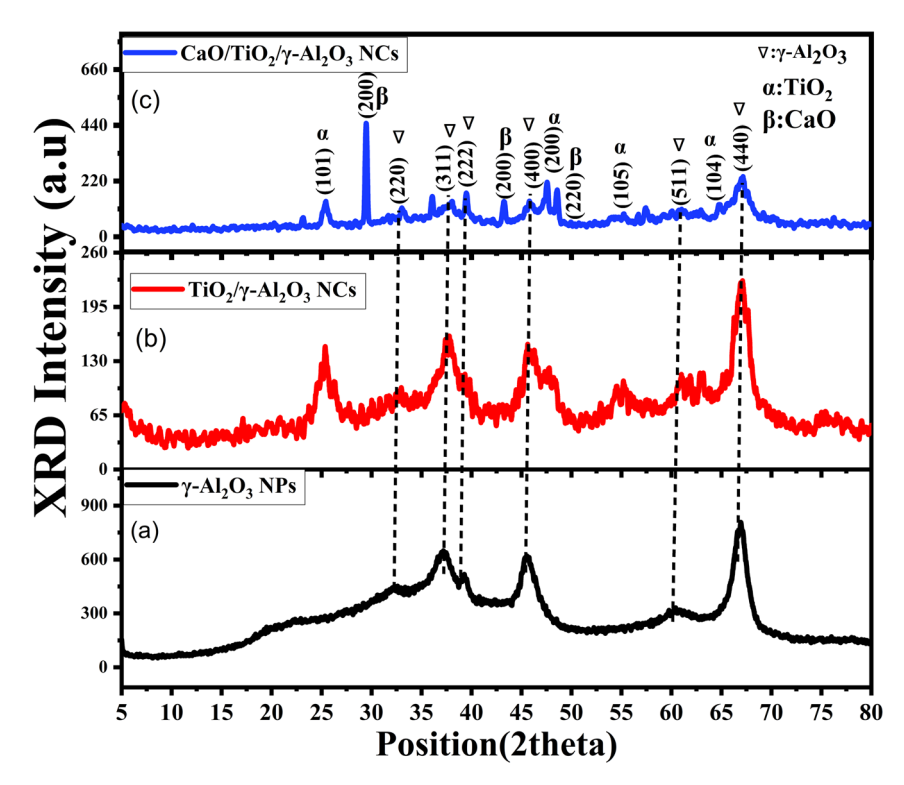


Fig. 1 XRD pattern: (a) γ -Al₂O₃ NPs, (b) TiO₂/ γ -Al₂O₃ NCs, and (c) CaO/TiO₂/ γ -Al₂O₃ NCs.

Table 1 Structural properties of synthesized metal oxide NPs and NCs

| Catalyst used | TEM (nm) | XRD (nm) | |
|--|-------------------------------|-------------|--|
| γ -Al $_2$ O $_3$ NPs | 9.55 \pm 1.2 nm | 3.2 ± 1.4 | |
| TiO ₂ /γ-Al ₂ O ₃ NCs | $7.60 \pm 0.9 \; \mathrm{nm}$ | 2.4 ± 0.8 | |
| $CaO/TiO_2/\gamma$ - Al_2O_3 NCs | 8.21 ± 2.1 | 2.7 ± 0.5 | |

prepared samples were irregular in shape with more agglomeration, which might point to the combination of CaO and TiO_2 into γ -Al₂O₃ NPs. These results are also in line with previous studies. ^{9,45} Fig. 3a–c illustrates the presence of porosity, which is considered one of the significant characteristics for photocatalyst activity. As shown by previous research studies, it increases the surface area, which plays a vital role in enhancing the catalytic performance. In addition, the stability and reusability of the catalysts can be enhanced by porosity. ^{46,47} Furthermore, Fig. 3d presents the EDX spectra that reveal the presence of Ca, O, Ti and Al in the synthesized CaO/TiO₂/ γ -Al₂O₃ NCs, reflecting the formation of CaO/TiO₂/ γ -Al₂O₃ NCs. The presented SEM images were in good agreement with the TEM results (Fig. 2).

3.4 FTIR analysis

FTIR analysis of the calcined γ -Al₂O₃ NPs, TiO₂-Al₂O₃ NCs, and CaO/TiO₂/ γ -Al₂O₃ NCs at 500 °C was carried out. Fig. 1 shows the FTIR pattern of synthesized NPs and NCs. It can be seen in the FITR of γ -Al₂O₃ NPs and TiO₂/Al₂O₃ NCs that the bands observed at around 3449.8 cm⁻¹ assigned to the O–H stretching bands indicate the occurrence of surface hydroxyl groups or

adsorbed moisture. This peak is usually broad due to hydrogen bonding between the hydroxyl groups, as reported in many previous studies. Similarly, the bands around 1628.6 cm $^{-1}$ can be attributed to O–H bending vibrations. Furthermore, the bands at 550–800 cm $^{-1}$ are associated with the vibrational stretching modes of the Al–O, Ti–O, and Ca–O bonds in the oxide lattice. Importantly, the FTIR spectra of CaO/TiO $_2/\gamma$ -Al $_2O_3$ showed similar absorption bands corresponding to hydroxyl groups (O–H stretching at 3434.59 cm $^{-1}$). Peaks were observed at 1389.3 cm $^{-1}$, indicating the presence of calcium carbonate due to the reaction with CO $_2$. The FTIR spectra of CaO–TiO $_2$ - γ -Al $_2O_3$ NCs show a strong basic property at 1500 cm $^{-1}$, which can be linked to the absorption of CO $_2$ from the atmosphere. This indicates the alteration of CaO and TiO into γ -Al $_2O_3$. Our FTIR results were in agreement with earlier studies. 29,45,48

3.5 Raman analysis

The Raman pattern of the calcined γ-Al₂O₃ NPs, TiO₂/γ-Al₂O₃ NCs, and CaO/TiO₂/γ-Al₂O₃ NCs are presented in Fig. 5. As observed, the γ -Al₂O₃ NPs display peaks at around 276.5 cm⁻¹, which is attributed to the O-Al-O bending mode. Furthermore, peaks at around 563.5 cm⁻¹ and 695.1 cm⁻¹ are determined to be Al-O stretching, in accordance with the formation of γ-Al₂O₃ NPs.49 Moreover, the Raman spectra of TiO₂/γ-Al₂O₃ NCs exhibited new peaks at 145.6 cm⁻¹, 563.5 cm⁻¹, and 691 cm⁻¹, as a similar reported study.50 The Raman shifts demonstrate the interactions at the interface of TiO2 and γ-Al2O3. Additionally, peaks at 1095.1 cm⁻¹ and 2418.8 cm⁻¹ could be caused by the stretching vibration of O-H. Likewise, CaO/TiO₂/γ-Al₂O₃ NCs present peaks 145.6 $cm^{-1},276.5$ cm^{-1} .

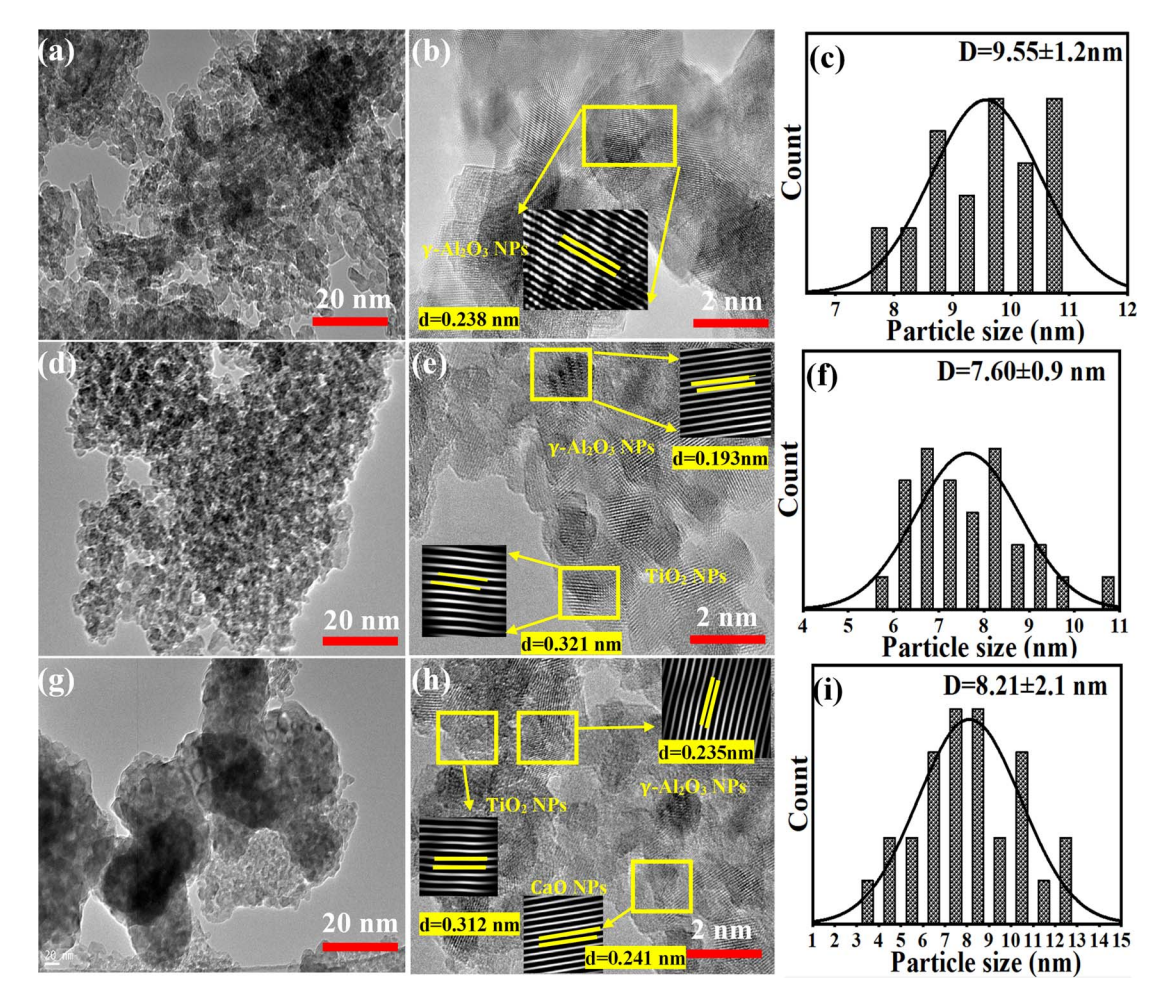


Fig. 2 TEM and HRTEM images, and particle size: (a-c) pure γ -Al₂O₃ NPs, (d-f) TiO₂/ γ -Al₂O₃ NPs, and (g-i) CaO/TiO₂/ γ -Al₂O₃ NCs.

563.5 cm⁻¹,691 cm⁻¹,784.3 cm⁻¹, 1095.1 cm⁻¹ and 2429 cm⁻¹. The primary Raman active mode of CaO is detected at around 710 cm⁻¹, arising from the stretching vibrations of the Ca–O bond.⁵¹ Nevertheless, the high peak intensities could be attributed to the crystallinity quality of CaO/TiO₂/ γ -Al₂O₃ NCs. The combined spectrum allows for the identification of all three components, verifying the successful synthesis of the NPs and NCs. These results agreed with the FTIR data (Fig. 4).

3.6 UV-Vis and PL study

The UV-vis absorption spectra of γ -Al₂O₃ NPs, TiO₂/ γ -Al₂O₃ NCs and CaO/TiO₂/ γ -Al₂O₃ NCs are presented in Fig. 6a. An absorption peak at 380 nm was recorded, indicating the formation of γ -Al₂O₃ NPs, which is in good agreement with recent studies. ^{52,53} CaO/TiO₂/ γ -Al₂O₃ NCs exhibited higher absorption intensity compared to both γ -Al₂O₃ NPs and TiO₂/ γ -Al₂O₃ NCs, demonstrating superior photocatalytic performance under UV irradiation. From the absorption spectra, the optical band gap energies were estimated to be 3.30 eV, 3.00 eV and 3.73 eV for γ -Al₂O₃ NPs, TiO₂/ γ -Al₂O₃ NCs, and CaO/TiO₂/ γ -Al₂O₃ NCs, respectively.

In addition, PL analysis was performed for $\gamma\text{-}Al_2O_3$ NPs, TiO $_2/\gamma\text{-}Al_2O_3$ NCs, and CaO/TiO $_2/\gamma\text{-}Al_2O_3$ NCs to understand the

electronic and optical properties at an excitation wavelength of 355 nm. As shown in Fig. 6b, the higher intensity for γ -Al₂O₃ NPs occurred at 406.2 nm with band-to-band transitions, in agreement with earlier studies. Shoulder peaks occurred at 425.1 nm and 477.9 nm, which could be linked to oxygen vacancies or aluminum-related defects. The peak that appeared at 523.5 nm could be related to transitions involving defect states. However, the intensity of the peaks of TiO₂/ γ -Al₂O₃ NCs was higher than those of γ -Al₂O₃ NPs. Similarly, TiO₂/ γ -Al₂O₃ and CaO/TiO₂/ γ -Al₂O₃ NCs exhibited the same peaks of γ -Al₂O₃ NPs. However, the intensity was higher than γ -Al₂O₃ NPs and TiO₂/ γ -Al₂O₃ NCs might be bound to Ti⁺³ ions. These finding shows that the composite with CaO and TiO₂ improves the PL properties of γ -Al₂O₃ NPs, making it beneficial for catalyst applications.

3.7 Zeta potential analysis

Dynamic light scattering (DLS) determines the particle distribution, surface charge, and stability of synthesized samples. Fig. 7a shows the particle distribution of the synthesized samples. It can be observed that the average particle distribution of the synthesized $\gamma\text{-Al}_2O_3$ NPs, $\text{TiO}_2/\gamma\text{-Al}_2O_3$ NPs, and CaO/TiO $_2/\gamma\text{-Al}_2O_3$ NCs were found to be 190.2 \pm 68.1 nm, 180.5 \pm 90.3 nm, and 188.2 \pm

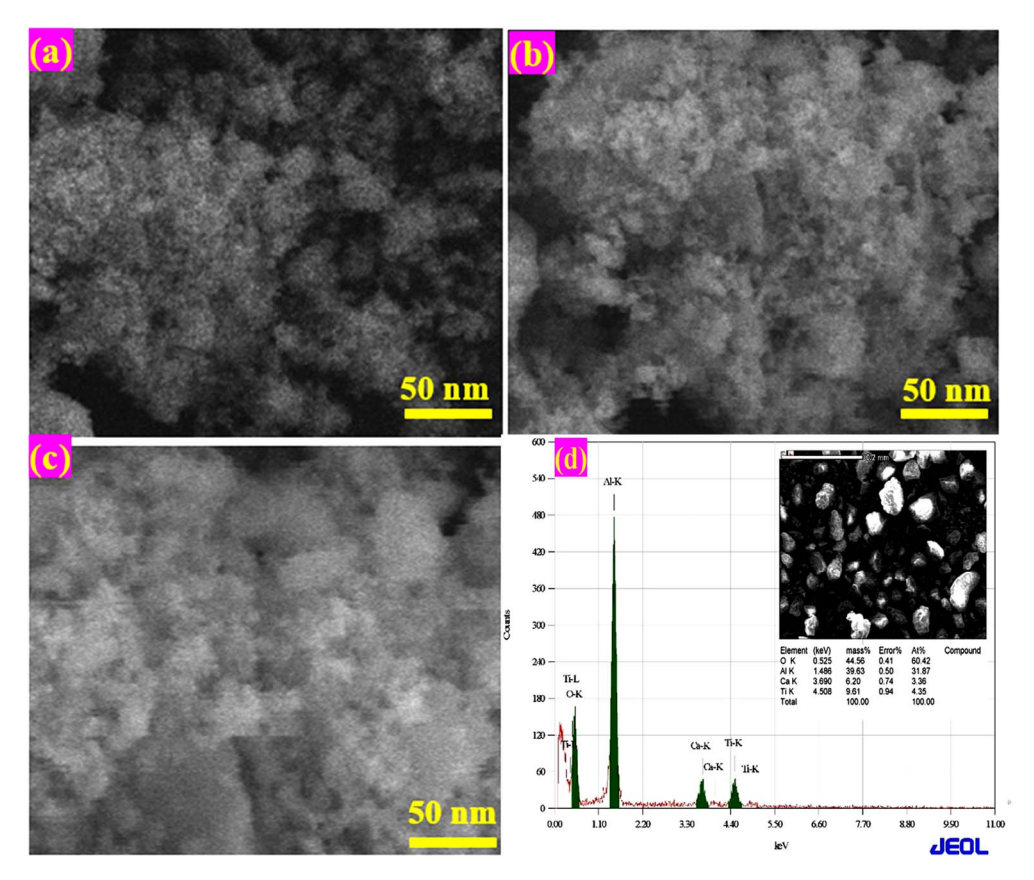


Fig. 3 SEM Analysis: (a) SEM image of γ -Al₂O₃ NPs, (b) TiO₂/ γ -Al₂O₃ NPs, (c) CaO/TiO₂/ γ -Al₂O₃ NCs. (d) EDX spectra of CaO/TiO₂/ γ -Al₂O₃ NCs.

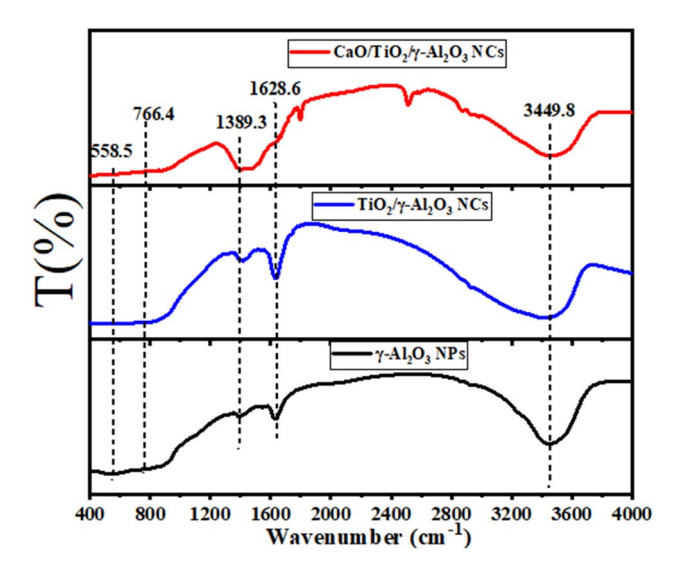


Fig. 4 FTIR spectra of γ –Al $_2O_3$ NPs, TiO $_2/\gamma$ –Al $_2O_3$ NCs, and CaO/TiO $_2/\gamma$ –Al $_2O_3$ NCs.

75.0 nm, respectively, as shown in Table 2. These results were supported by TEM data (Fig. 2). Moreover, the surface charge was measured to evaluate the stability of the three samples, which is critical for catalytic applications. The zeta potential of γ -Al₂O₃ is highly pH-dependent due to the ionization of the surface hydroxyl groups. As represented in Fig. 4a, the zeta potential value of γ -

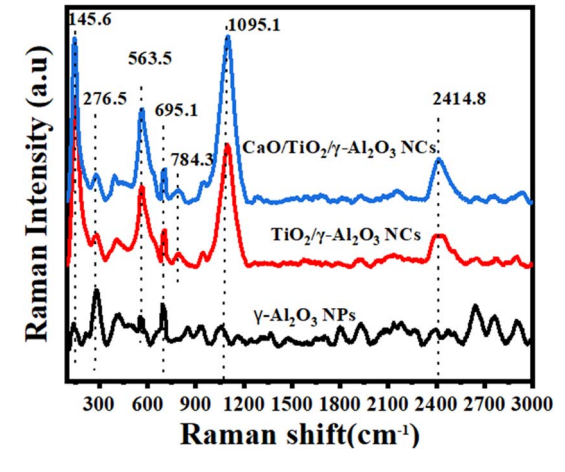


Fig. 5 Raman spectra of γ -Al $_2O_3$ NPs, TiO $_2/\gamma$ -Al $_2O_3$ NCs, and CaO/TiO $_2/\gamma$ -Al $_2O_3$ NCs.

Al $_2$ O $_3$ NPs was found to be -11.2 ± 16.6 mV, which could define the amorphous phase of γ -Al $_2$ O $_3$ NPs. 57 This zeta potential result might also be correlated with the aggregation of the sample during synthesis. In contrast, the zeta potential of TiO $_2$ / γ -Al $_2$ O $_3$ NCs was -26.5 ± 6.5 mV, indicating better stability than γ -Al $_2$ O $_3$ NPs (Fig. 4b). 44 Furthermore, the zeta potential of CaO/TiO $_2$ / γ -Al $_2$ O $_3$ nanocomposites (NCs) was -28.9 ± 4.3 mV, signifying a high surface charge due to the incorporation of CaO, as

Paper RSC Advances

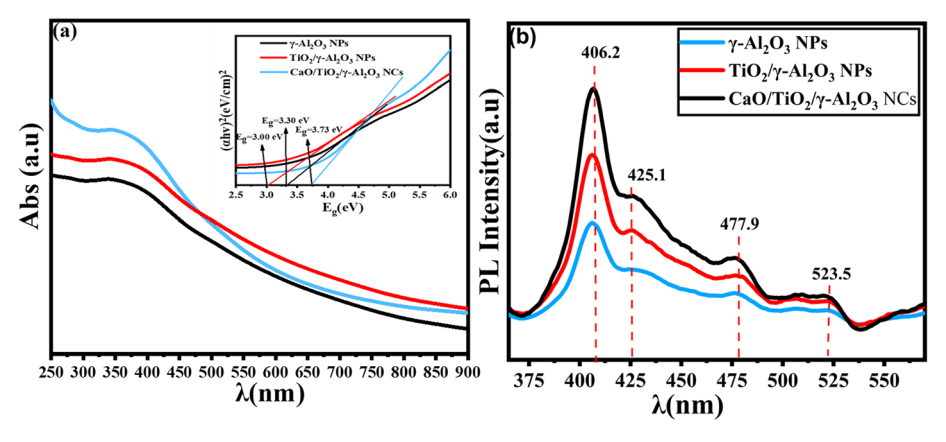


Fig. 6 (a) UV-Vis pattern and (b) PL pattern of the prepared γ -Al₂O₃ NPs, TiO₂/ γ -Al₂O₃ NCs, and CaO/TiO₂/ γ -Al₂O₃ NCs.

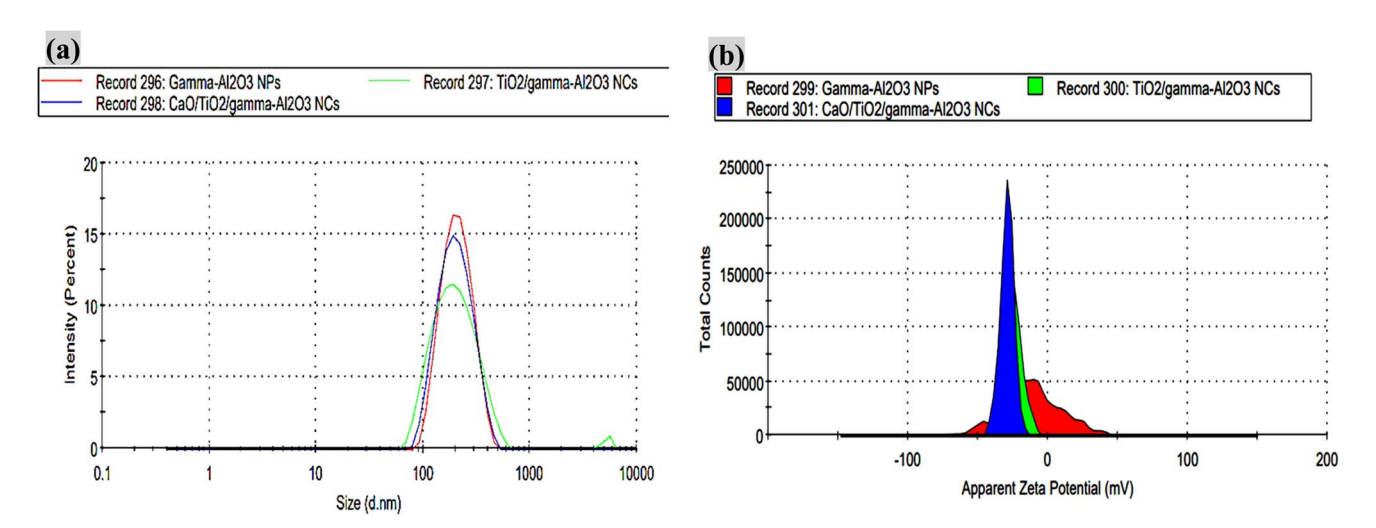


Fig. 7 (a) Particle distribution and (b) zeta potential analysis for the prepared γ -Al₂O₃ NPs, TiO₂/ γ -Al₂O₃ NCs, and CaO/TiO₂/ γ -Al₂O₃ NCs.

illustrated in Fig. 4c. Understanding the zeta potential of the NP and NCs samples is fundamental for their application in catalysis, adsorption processes, and as support materials in heterogeneous catalysis, as it impacts the particle dispersion and reactivity.

3.8 Photocatalytic evaluation

The photocatalysis studies of the MB dye using pure γ -Al₂O₃ NPs, TiO₂/ γ -Al₂O₃ NCs, and CaO/TiO₂/ γ -Al₂O₃ NCs were carried out under direct UV light for 200 min (Fig. 8a–f). As can be observed in Fig. 8a, the UV absorption of γ -Al₂O₃ NPs decreased with increasing exposure time. Moreover, a notable reduction of the UV absorption was achieved for TiO₂/ γ -Al₂O₃ NCs for a duration of 200 min (Fig. 8b). Additionally, a significant decrease in the UV absorption of CaO/TiO₂/ γ -Al₂O₃ NCs was

detected with an expansion in the duration time (Fig. 8c). This observation of CaO/TiO₂/ γ -Al₂O₃ NCs signifies the essential impact of the sample in breaking down organic pollutants. Correspondingly, Fig. 8e demonstrates the constant rates of 0.0027 min⁻¹, 0.0074 min⁻¹ and 0.0140 min⁻¹ for γ -Al₂O₃ NPs, TiO₂/ γ -Al₂O₃ NCs and CaO/TiO₂/ γ -Al₂O₃ NCs, respectively. As shown in the results, the high color of the MB solution was rapidly degraded with the CaO/TiO₂/ γ -Al₂O₃ NCs compared to the individual samples. Moreover, Fig. 8f displays the degradation efficiency of the prepared samples, which was 45% for γ -Al₂O₃ NPs, 79% for TiO₂/ γ -Al₂O₃ NCs, and 94.1% for CaO/TiO₂/ γ -Al₂O₃ NCs, respectively. These values showed that the addition of CaO and TiO₂ into γ -Al₂O₃ plays a role in enhanced photocatalytic degradation (Table 3).

Table 2 Summary of the DLS data of the prepared γ -Al₂O₃ NPs, TiO₂/ γ -Al₂O₃ NCs, and CaO/TiO₂/ γ -Al₂O₃ NCs

| Sample used | Particle size (nm \pm SD) | Zeta potential (mV \pm SD) |
|---|------------------------------------|----------------------------------|
| γ -Al ₂ O ₃ NPs TiO ₂ / γ -Al ₂ O ₃ NCs | $190.2 \pm 68.1 \\ 180.5 \pm 90.3$ | $-11.2 \pm 16.6 \ -26.5 \pm 6.5$ |
| CaO/TiO ₂ /γ-Al ₂ O ₃ NCs | 188.2 ± 75.0 | -28.9 ± 4.3 |

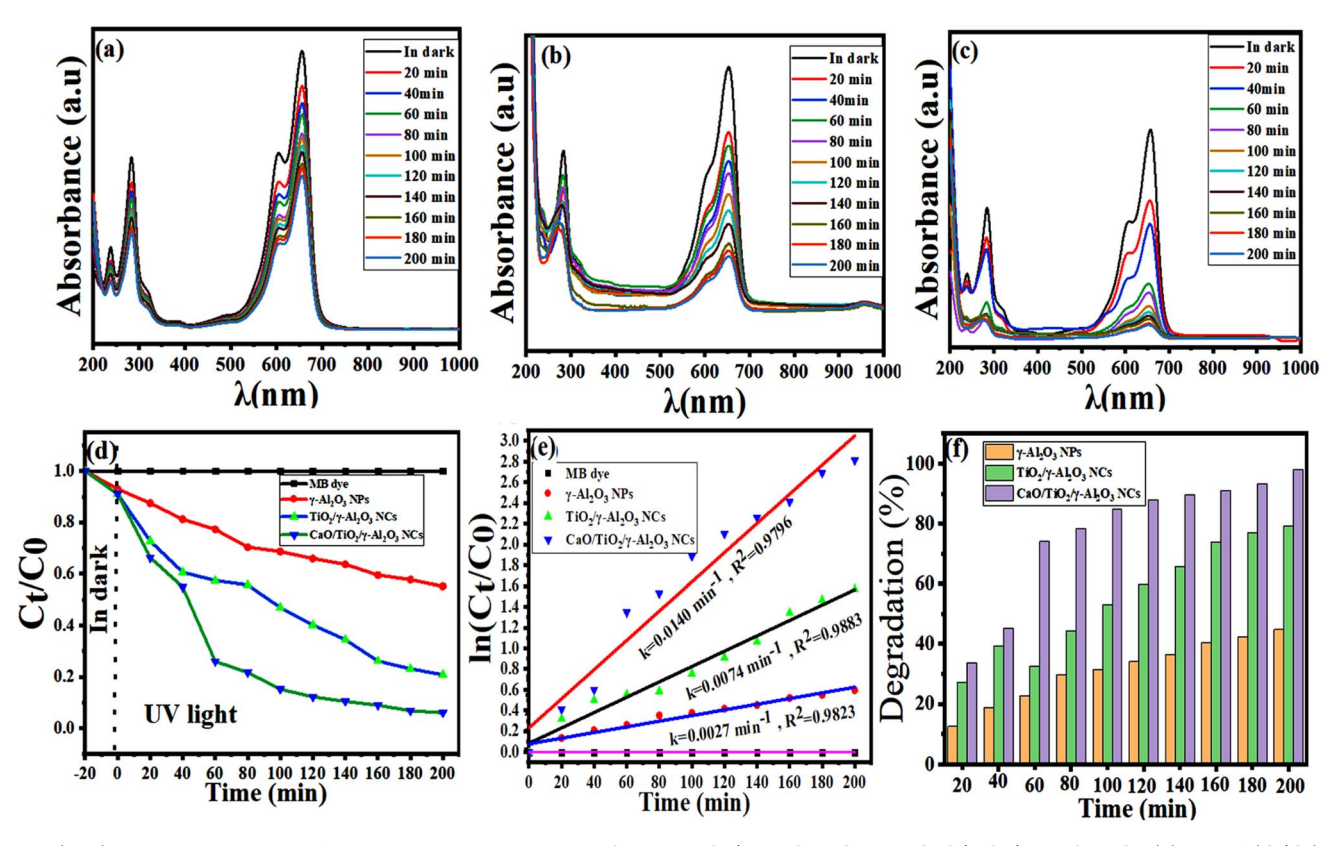


Fig. 8 (a–c) UV-Vis absorbance of the MB dye solution by γ -Al₂O₃ NPs, TiO₂/ γ -Al₂O₃ NCs, and CaO/TiO₂/ γ -Al₂O₃ NCs. (d) Plot of (C_t/C_0) vs. irradiation time (min), (e) kinetics of the photocatalysis of the MB solutions for the prepared samples, and (f) degradation efficiency (D%) of the MB solution using the synthesize d catalyst.

3.8.1 The recycling stability of the catalyst. In this investigation, the same CaO/TiO₂/ γ -Al₂O₃ NCs were used to degrade MB dye under UV irradiation to evaluate its stability and the recycling potential of the photocatalysts. Without any additional processing, the CaO/TiO₂/ γ -Al₂O₃ NCs were recycled four times under the same conditions using centrifugation. Fig. 9 shows the recycling stability of the prepared CaO/TiO₂/ γ -Al₂O₃ NCs over four cycles of photocatalytic degradation. As observed in the results, the degradation efficiency remains high throughout the cycles, with only a slight decrease from 94.1% in the first cycle to 92.1% in the fourth cycle. This phenomenon demonstrates the excellent stability and reuse potential of the prepared NCs. This work suggests that the CaO/TiO₂/ γ -Al₂O₃ nanocomposites (NCs) could be utilized in potential applications, such as environmental remediation and medical therapy.

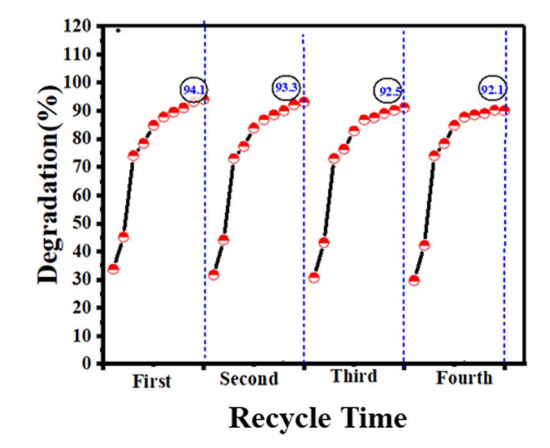


Fig. 9 Recycling stability of the synthesized CaO/TiO $_2$ / γ -Al $_2$ O $_3$ NCs.

Table 3 Comparison of the degradation efficiency between the presented samples and previous different samples

| Sample used | Experimental conditions | Irradiation time (min) | Degradation target | Degradation efficiency (%) | Ref. |
|--|-------------------------|---------------------------|-----------------------|----------------------------|------------|
| CaO/TiO ₂ /γ-Al ₂ O ₃ NCs | UV light | 200 | MB | 94.1% | This study |
| Au/BiOBr/graphene | Visible light | 180 | Phenol | 64% | 6 |
| MgO/Fe ₂ O ₃ /γ-Al ₂ O ₃ NCs | UV light | 140 | MB | 90.4% | 9 |
| Mn-S co-doped TiO ₂ NCs | Sun light | 120 | Phenol | 59% | 58 |
| α-Fe ₂ O ₃ /ZnO NCs | UV light | 120 | MB | 91.6% | 59 |
| CuO/MoS ₂ @gCN NCs | UV light | 35 | Phenol | 63.50% | 60 |
| Nb(2.0)/TiO ₂ | UV | 160 | Phenol | 94% | 61 |
| nanocomposite | | | | | |

Paper

Fig. 10 Possible mechanism of the decomposition of the MB dye using the prepared $CaO/TiO_2/\gamma$ - Al_2O_3 NCs.

3.8.2 Mechanism of the photodegradation of the MB dye.g. 10 describes a schematic representation of the proposed

Fig. 10 describes a schematic representation of the proposed mechanism for the degradation of MB dye using the prepared CaO/TiO₂/γ-Al₂O₃ NCs. There is a different probable mechanism of degradation of the MB dye as follows. Initially, when the NCs are exposed to UV irradiation, the electron in CaO absorbs photons and is excited from the valence band (VB) to the conduction band (CB), as shown in eqn (3). Those electrons (e⁻) will then transfer to TiO_2 and are later transferred to γ -Al₂O₃, leaving holes (h⁺) that will then transfer to γ -Al₂O₃, as illustrated in eqn (4) and (5). After that, these electrons (e⁻) subsequently reduce oxygen molecules to generate superoxide anions 'O2' and the holes oxide hydroxide ions to form hydroxyl radical 'OH as demonstrated in eqn (6) and (7), respectively. Furthermore, these 'OH strike the phenol molecules and decompose them down into smaller intermediates, therefore generating compounds such as CO₂ and H₂O, as shown in eqn (8).⁶² The reaction process is described in the following equations.

CaO/TiO₂/
$$\gamma$$
-Al₂O₃ NCs + $h\nu \rightarrow$
CaO/TiO₂/ γ -Al₂O₃ NCs (h⁺ + e⁻) (4)

$$CaO(e^{-}) \rightarrow TiO_{2}(e^{-})$$
 (5)

$$TiO_2 (e^-) \rightarrow \gamma - Al_2O_3 (e^- \text{ defect site})$$
 (6)

$$\gamma - Al_2O_3 (e^-) + O_2 \rightarrow 'O_2^-$$
 (7)

$$\gamma$$
-Al₂O₃ (h⁺) + OH⁻ \rightarrow 'OH (8)

$$({}^{\cdot}O_2^{-} \text{ and } {}^{\cdot}OH) + MB \text{ dye } \rightarrow CO_2 + H_2O$$

4. Conclusion

This work successfully fabricated $\text{CaO/TiO}_2/\gamma\text{-Al}_2\text{O}_3$ NCs via the one-step co-precipitation route with superior photocatalytic activity. The characterization analysis included studies focused on

the structural, morphological, optical, and stability of the synthesised samples, and was accomplished using XRD, TEM, SEM, EDX, Raman, FTIR, PL, and DLS spectroscopy. XRD data reveal the enhanced crystallinity structure and phase purity with the addition of CaO and TiO₂ into γ-Al₂O₃ NPs. TEM analysis of the prepared samples shows a spherical shape with less agglomerations of particles and a particle size of 8.21 \pm 2.1 nm after the addition of CaO NPs. The percentages of elements (Ca, Ti, Al, and O) in the prepared CaO/TiO₂/γ-Al₂O₃ NCs were confirmed through EDX spectra. The bonds and functional groups within molecules of the prepared samples were determined from Raman and FTIR spectra. Optical properties that determine the recombination of electron-hole pairs are revealed through PL analysis. DLS data show that the average particle distribution of the synthesized γ -Al₂O₃ NPs, TiO₂/γ-Al₂O₃ NCs, and CaO/TiO₂/γ-Al₂O₃ NCs was found to be 190.2 \pm 68.1 nm, 180.5 \pm 90.3 nm, and 188.2 \pm 75.0 nm, respectively. Moreover, the zeta potential of the samples decreased from -11.2 ± 16.6 mV to -28.9 ± 4.3 mV with the addition of the supporting TiO2 and CaO NPs. Photocatalytic experiments show that under irradiation by UV light for 200 min, the CaO/TiO₂/Al₂O₃ NCs achieved the highest degradation efficiency (98%) of the MB dye compared to the individual samples. These results indicate that the addition of TiO₂ and CaO NPs into γ -Al₂O₃ improved the photocatalytic performance due to their high surface area and promoted charge separation. This study suggests that synthesized CaO/TiO₂/γ-Al₂O₃ NCs can be applied to sustainable solutions in wastewater treatment and other environmental applications.

Data availability

The data in this work are obtained from the corresponding author upon reasonable request.

Author contributions

This work was performed by Emaan Alsubhe.

Conflicts of interest

The authors confirm that the work presented here is original research and has not been submitted for publication elsewhere.

Acknowledgements

The author is grateful for research support from Taibah University.

References

- 1 C. Martinez-Gómez, I. Rangel-Vazquez, R. Zarraga, G. Del Ángel, B. Ruíz-Camacho, F. Tzompantzi, E. Vidal-Robles and A. Perez-Larios, *Processes*, 2022, **10**(6), 1186.
- 2 F. T. Li, Y. Zhao, Y. J. Hao, X. J. Wang, R. H. Liu, D. S. Zhao and D. M. Chen, *J. Hazard. Mater.*, 2012, **239–240**, 118–127.
- 3 A. A. Ismail, I. Abdelfattah, M. F. Atitar, L. Robben, H. Bouzid, S. A. Al-Sayari and D. W. Bahnemann, Sep. Purif. Technol., 2015, 145, 147–153.
- 4 J. J. Rueda-Marquez, I. Levchuk, P. Fernández Ibañez and M. Sillanpää, *J. Cleaner Prod.*, 2020, 258, 120694.
- 5 M.-J. Zhou, W.-T. Zhang, Z. Li, T. Feng, S. Lan, Z. Peng and S.-Q. Chen, *Rare Met.*, 2023, 42, 3443–3454.
- 6 R. Kaveh and H. Alijani, J. Asian Ceram. Soc., 2021, 9, 343–365.
- 7 X. Li, H. Zhou, R. Qian, X. Zhang and L. Yu, *Chin. Chem. Lett.*, 2025, **36**, 110036.
- 8 A. Sridevi, S. Krishnamohan, M. Thairiyaraja, B. Prakash and R. Yokeshwaran, *Inorg. Chem. Commun.*, 2022, **138**, 109311.
- 9 Z. A. M. Alaizeri, H. A. Alhadlaq, S. Aldawood and M. Ahamed, *Catalysts*, 2024, **14**(12), 923.
- 10 Z. Algarni, Res. Chem. Intermed., 2025, 1-24.
- 11 I. Ahmad, Y. Zou, J. Yan, Y. Liu, S. Shukrullah, M. Y. Naz, H. Hussain, W. Q. Khan and N. R. Khalid, *Adv. Colloid Interface Sci.*, 2023, 311, 102830.
- 12 P. Mallick, S. K. Sahoo and S. K. Satpathy, *J. Mol. Liq.*, 2024, **406**, 125071.
- 13 Z. Cheng, S. Zhao and L. Han, *Nanoscale*, 2018, **10**, 6892–6899.
- 14 I. Koltsov, G. Kimmel, S. Stelmakh, K. Sobczak and W. Lojkowski, *Sci. Rep.*, 2019, **9**(1), 5540.
- S. Islak, S. Buytoz, E. Ersoz, N. Orhan, J. Stokes,
 M. S. J. Hashmi, I. Somunkiran and N. Tosun,
 Optoelectron. Adv. Mater., Rapid Commun., 2012, 610, 844–849.
- 16 D. Oh, Y.-R. Jo, J. Chang, H. An, H. J. Kim, J. M. Vohs, W. Jung and S. Lee, ACS Appl. Mater. Interfaces, 2024, 16, 64714– 64724.
- 17 A. Sridevi, S. Krishnamohan, M. Thairiyaraja, B. Prakash and R. Yokeshwaran, *Inorg. Chem. Commun.*, 2022, **138**, 109311.
- 18 Y. E. Kim, W. Lee, M. H. Youn, S. K. Jeong, H. J. Kim, J. C. Park and K. T. Park, J. Ind. Eng. Chem., 2019, 78, 73–78.
- 19 D. Huang, W. Xie, Z. Tu, F. Zhang, S. Quan and L. Liu, *J. Nanosci. Nanotechnol.*, 2013, 13(1), 260–269.
- 20 W. Mahdi, A. Flayyih and F. Musa, *J. Kim. Valensi*, 2024, **10**(2), 277–289.

- 21 R. Dubadi, E. Weidner, B. Samojeden, T. Jesionowski, F. Ciesielczyk, S. Huang and M. Jaroniec, *Molecules*, 2023, 28(5), 2002.
- 22 R. J. Kudla, S. Subramanian, M. S. Chattha and T. E. Hoost, *Ind. Eng. Chem. Res.*, 1996, 35, 4394–4397.
- 23 C.-S. Lee, H. Rho, N. Sharma, B. Jung and P. Westerhoff, *ACS ES& T Water*, 2023, 3(8), 2481–2490.
- 24 M. Jeevarathinam and I. V. Asharani, Sci. Rep., 2024, 14(1), 9718.
- 25 H. Derikvandi and A. Nezamzadeh-Ejhieh, *J. Colloid Interface Sci.*, 2017, **490**, 314–327.
- 26 A. Kanwal, S. Sajjad, S. A. K. Leghari and M. N. Khan, *Chin. J. Chem. Eng.*, 2021, 147–159.
- 27 T. Jan, S. Azmat, Q. Mansoor, H. M. Waqas, M. Adil, S. Z. Ilyas, I. Ahmad and M. Ismail, *Microb. Pathog.*, 2019, 134, 103579.
- 28 A. M. Rheima, A. A. Anber, H. I. Abdullah and A. H. Ismail, *Nano Biomed. Eng.*, 2021, **13**, 1–5.
- 29 K. Atrak, A. Ramazani and S. Taghavi Fardood, *J. Mater. Sci.: Mater. Electron.*, 2018, **29**, 8347–8353.
- 30 S. Mahshid, M. Askari, M. Sasani Ghamsari, N. Afshar and S. Lahuti, *J. Alloys Compd.*, 2009, **478**, 586–589.
- 31 T. Theivasanthi and M. Alagar, Titanium dioxide (TiO₂) Nanoparticles-XRD Analyses-An Insight, *arXiv*, 2013, preprint arXiv:1307.1091, DOI: 10.48550/arXiv.1307.1091.
- 32 M. J. Valero-Romero, J. G. Santaclara, L. Oar-Arteta, L. van Koppen, D. Y. Osadchii, J. Gascon and F. Kapteijn, *Chem. Eng. J.*, 2019, **360**, 75–88.
- 33 T. N. Blanton and C. L. Barnes, Quantitative Analysis Of Calcium Oxide Desiccant Conversion To Calcium Hydroxide Using X-Ray Diffraction.
- 34 M. Galván-Ruiz, J. Hernández, L. Baños, J. Noriega-Montes and M. E. Rodríguez-García, *J. Mater. Civ. Eng.*, 2009, 21(11), 694–698.
- 35 A. Roy and J. Bhattacharya, *Int. J. Nanosci.*, 2012, **11**(5), DOI: **10.1142/S0219581X12500275**.
- 36 Y. Rozita, R. Brydson and A. Scott, 2010.
- 37 P. Arunarajeswari, T. Mathavan, A. Divya and A. M. F. Benial, *Mater. Res. Express*, 2020, **6**(12), 1250c9.
- 38 K. Loza, M. Epple and M. Maskos, *Biological Responses to Nanoscale Particles: Molecular and Cellular Aspects and Methodological Approaches*, 2019, pp. 85–100.
- 39 B. R. Cuenya, Thin Solid Films, 2010, 518(12), 3127-3150.
- 40 I. Limón-Rocha, A. Marizcal-Barba, C. A. Guzmán-González, L. M. Anaya-Esparza, S. Ghotekar, O. A. González-Vargas and A. Pérez-Larios, *Inorganics*, 2022, 10(10), 157.
- 41 A. Esfandyari Bayat, R. Junin, S. Shamshirband and W. Tong Chong, *Sci. Rep.*, 2015, 5(1), 14264.
- 42 S. A. Hassanzadeh-Tabrizi, J. Alloys Compd., 2023, 968, 171914.
- 43 Y. Q. Cheng and E. Ma, *Prog. Mater. Sci.*, 2011, **56**(4), 379–473.
- 44 Z. A. M. Alaizeri, H. A. Alhadlaq, S. Aldawood and N. A. Y. Abduh, *RSC Adv.*, 2024, **14**, 16685–16695.
- 45 M. Mohamad, N. Ngadi, S. Wong, N. Y. Yahya, I. M. Inuwa and N. S. Lani, *Int. J. Eng., Trans. B*, 2018, **31**, 1326–1333.

Paper

46 A. P. Naik, H. Mittal, V. S. Wadi, L. Sane, A. Raj, S. M. Alhassan, A. Al Alili, S. V. Bhosale and P. P. Morajkar, J. Environ. Manage., 2020, 258, 110029.

- 47 P. Deka, R. C. Deka and P. Bharali, *New J. Chem.*, 2016, **40**, 348–357.
- 48 Y. Tang, G. Chen, J. Zhang and Y. Lu, *Bull. Chem. Soc. Ethiop.*, 2011, 25, 37–42.
- 49 I. González De Arrieta, A. Zaki, A. Canizarès, E. Véron,
 C. Genevois, L. Del Campo, C. Blanchard and
 O. Rozenbaum, Spectrochim. Acta, Part A, 2023, 298, 122795.
- 50 S. Gullapelli, M. S. Scurrell and D. K. Valluri, *Int. J. Hydrogen Energy*, 2017, 42, 15031–15043.
- 51 T. Schmid and P. Dariz, J. Raman Spectrosc., 2014, 46(1).
- 52 A. H. Gharbi, S. E. Laouini, H. Hemmami, A. Bouafia, M. T. Gherbi, I. Ben Amor, G. G. Hasan, M. M. S. Abdullah, T. Trzepieciński and J. A. A. Abdullah, *Coatings*, 2024, 14(7), 848.
- 53 P. Manogar, J. Esther Morvinyabesh, P. Ramesh, G. Dayana Jeyaleela, V. Amalan, J. S. Ajarem, A. A. Allam, J. Seong Khim and N. Vijayakumar, *Mater. Lett.*, 2022, 311, 131569.

- 54 R. Gayathri, G. Raja and P. Rajeswaran, *J. Mater. Sci.: Mater. Electron.*, 2020, **31**, 9742–9752.
- 55 P. A. Prashanth, R. S. Raveendra, R. Hari Krishna, S. Ananda, N. P. Bhagya, B. M. Nagabhushana, K. Lingaraju and H. Raja Naika, J. Asian Ceram. Soc., 2015, 3, 345–351.
- 56 Y. X. Zhang, G. H. Li, Y. X. Jin, Y. Zhang and J. Zhang, *Chem. Phys. Lett.*, 2002, **365**(3–4), 300–304.
- 57 J. Ji, X. Yao, J. Gao, W. Lu, W. Wang and D. Chu, *Chem. Phys. Lett.*, 2021, **781**, 138996.
- 58 A. Siddiqa, S. Haider, M. Mushtaq, S. Farooq and S. Shahida, *J. Dispersion Sci. Technol.*, 2025, 1–18.
- 59 A. Noruozi and A. Nezamzadeh-Ejhieh, *Chem. Phys. Lett.*, 2020, 752, 137587.
- 60 N. Alomayrah, M. Ikram, S. Alomairy, M. S. Al-Buriahi, M. Naziruddin Khan, M. Farooq Warsi and A. Irshad, *Results Phys.*, 2024, 64, 107902.
- 61 N. Almulhem, C. Awada and N. M. Shaalan, *Crystals*, 2022, 12(7), 911.
- 62 N. S. Alsaiari, F. M. Alzahrani, A. Amari, H. Osman, H. N. Harharah, N. Elboughdiri and M. A. Tahoon, *Molecules*, 2023, 28(1), 463.